On the correlation between irradiation-induced microstructural features and the hardening of reactor pressure vessel steels

M. Lambrecht [a,b,*], E. Meslin [c,1], L. Malerba [a], M. Hernández-Mayoral [d], F. Bergner [e], P. Pareige [c], B. Radiguet [c], A. Almazouzi [a,2]

[a] Nuclear Materials Science Institute, SCK•CEN, Boeretang 200, 2400 Mol, Belgium
[b] Dep. of Materials Science and Engineering, UGent, Technologiepark 903, 9053 Ghent, Belgium
[c] Groupe de Physique des Matériaux UMR-CNRS 6634, Equipe de Recherche Technologique, No. 1000, Université de Rouen, B.P. 12, 76801 Saint Etienne du Rouvray, France
[d] CIEMAT, Division of Structural Materials, Avenida Complutense, 22. 28040-Madrid, Spain
[e] Forschungszentrum Dresden-Rossendorf, Institute of Safety Research, P.O. Box 510119, 01314 Dresden, Germany

ABSTRACT

A correlation is attempted between microstructural observations by various complementary techniques, which have been implemented within the PERFECT project and the hardening measured by tensile tests of reactor pressure vessel steel and model alloys after irradiation to a dose of $\sim 7 \times 10^{19}$ n cm^{-2}. This is done, using the simple hardening model embodied by the Orowan equation and applying the most suitable superposition law, as suggested by a parametric study using the DUPAIR line tension code. It is found that loops are very strong obstacles to dislocation motion, but due to their low concentration, they only play a minor role in the hardening itself. For the precipitates, the contrary is found, although they are quite soft (due to their very small sizes and their coherent nature), they still play the dominant role in the hardening. Vacancy clusters are important for the formation of both loops and precipitates, but they will play almost no role in the hardening by themselves.

© 2010 Elsevier B.V. All rights reserved.

1. Introduction

Irradiation-induced hardening and embrittlement of reactor pressure vessel (RPV) steels represent a great concern for nuclear power plant (NPP) life assessment. Therefore, these steels have been, since many years, the subject of extensive investigations (e.g. [1]). The cause of the hardening and embrittlement is currently accepted to be the irradiation-induced formation of copper-rich precipitates and matrix damage [2]. The latter probably consists of small voids and self-interstitial loops, associated or not with solute elements. Lumping voids and loops into a single category of hardening features corresponds, however, to a very crude approach, as they interact very differently with dislocations. Today, while the dominant role of copper-rich precipitates on hardening and embrittlement in steels with significant levels of copper is well documented [1–5], there is no clear perception of the whether it is the voids or loops that mainly contribute to the matrix hardening. The latter information may become of importance in connection with NPP lifetime extension, as it is known that, while the contribution to hardening of copper-rich precipitates saturates with dose, the contribution of matrix damage does not, at least in the range of dose of technological relevance [4].

One of the difficulties for the quantification of the effect on hardening of voids and loops is the fact that these defects are hard to detect in RPV steels. However, nowadays the progress achieved in advanced experimental techniques such as e.g. transmission electron microscopy (TEM) [6], positron annihilation spectroscopy (PAS) [7], atom-probe tomography (APT) [8] and Small Angle Neutron Scattering (SANS) [9], and their combined use, enables a detailed investigation of these irradiation-induced nano-features to be performed in RPV steels. Thereby, this investigation allows better establishing of the correlation of these features to the hardening and embrittlement.

In this study, based on the extensive joint work performed in different laboratories, considering the microstructural and mechanical characterization of model alloys and an RPV steel within the European project PERFECT [10], a first assessment has been attempted of the individual role of copper-rich precipitates, self-interstitial loops and voids on the hardening. First, a parametric study using a Foreman–Makin-type code [11] (the DUPAIR code [12,13], developed at

* Corresponding author at: Nuclear Materials Science Institute, SCK•CEN, Boeretang 200, 2400 Mol, Belgium. Tel.: +32 14 33 30 89; fax: +32 14 32 12 16.
E-mail addresses: Marlies.Lambrecht@SCKCEN.BE, mlambrec@sckcen.be (M. Lambrecht).
[1] Permanent address: Service de Recherches de Métallurgie Physique, CEA/Saclay, 91191 Gif-sur-Yvette cedex, France.
[2] Present address: EDF R&D renardières, 77250 Ecuelles, France.

EDF in the framework of the PERFECT project) is performed in order to establish, depending on the relative strength of the obstacles, whether a linear or a quadratic summation is more suitable to superpose the effects on hardening of different defect populations.

The validation of the model is made, by using the microstructural results obtained within the PERFECT project that are summarized in [14]. It was found that three different defect populations are observed, i.e. loops, vacancy clusters and precipitates. It should be mentioned that in this paper, the precipitates are defined as a kind of defects, as well. The classical Orowan equation is used to provide a first assessment of the strength of the different defect populations, and the results are superposed, according to the laws chosen in the first part, to fit the total measured hardening.

Finally, some conclusions are drawn and an outlook on future work is briefly given.

2. Superposition of the effect of different defect populations on yield strength increase

The 2D quasi-static code DUPAIR upgrades the algorithm, suggested by Foreman and Makin [11] by considering defect pinning forces as input parameter and by removing the constant line tension approximation, which is replaced by an expression explicitly dependent on the angle between the Burgers vector and the dislocation line [15]. Any kind of defect distributions, of different types and sizes, can be easily introduced, randomly distributed on a plane array (dislocation glide plane).

The application of a shear stress τ causes the segments of the single dislocation line to bow into a sequence of arcs of circles, each delimited by two pinning defects. The equilibrium shape of the dislocation line pinned between two defects is obtained setting the force balance at the pinning point between the two line tensions vectors $\overrightarrow{T_1}$ and $\overrightarrow{T_2}$ and the pinning force $\overrightarrow{F_p}$. The applied stress is increased until breakaway occurs at some defect. The shape of the dislocation line is then accordingly reconfigured and

the process of increasing the shear stress is restarted, till one of the two following breakaway criteria occurs.

(i) $\left|\overrightarrow{T_1} + \overrightarrow{T_2}\right| > \left|\overrightarrow{F_p}\right|$.

(ii) If the angle θ between the two dislocation braces becomes smaller than a critical value θ_c, the dislocation line unpins independently of the value of line tensions and pinning force (Orowan mechanism).

The highest shear stress applied during the simulation to allow the dislocation to move is taken as yield stress (YS) increase due to the array of obstacles. Therefore, a number of simulations must be performed in each case in order for the found average maximum value to have statistical significance. The global YS increase is finally estimated by multiplying the average maximum value by the Taylor factor, equal to 3.06. The effect of thermal activation on dislocation unpinning is also included in the code, by means of a simple model that can be found in, e.g. [15].

Here the DUPAIR code is utilized for a purely parametric study, with the aim to identify the best superposition law, used to obtain the effect of a number of different defect populations. In most mechanistic models, different hardening laws are associated with the microscopic mechanisms and the total yield strength increase ($\Delta\sigma_{tot}$) under irradiation is obtained as the superposition of the different effects (e.g. [16,17]). This superposition can be either linear (Eq. (1)), or as the square root of the quadratic sum (Eq. (2)) of the single components ($\Delta\sigma_i$).

$$\Delta\sigma_{tot}^L = \Delta\sigma_1 + \Delta\sigma_2 + \cdots \qquad (1)$$
$$\Delta\sigma_{tot}^Q = \sqrt{\Delta\sigma_1^2 + \Delta\sigma_2^2 + \cdots} \qquad (2)$$

Neither of these superposition laws is supported by any clear physical reason and it is expected that, in fact, in each case, depending on the involved defect populations, their density, their pinning forces, etc., the actual superposition should lie somewhere in between the two laws (Eq. (3)) [18]:

$$\Delta\sigma_{tot} = S \cdot \Delta\sigma_{tot}^L + (1 - S) \cdot \Delta\sigma_{tot}^Q \qquad (3)$$

Here, S is a superposition parameter that can vary in absolute value between 0 and 1 (0 corresponds to a purely quadratic sum, and 1 to a purely linear sum). The choice of the value of S is not settled, though. The DUPAIR code is adequate to perform an assessment of which one of the two laws (Eqs. (1) and (2)) should be used or, if neither proved acceptable, to give some indications about what value for S should be employed in each case.

Simulations were performed with two defect populations, one (weak defects) with a pinning force F_w varying from 0.2 to 1.5 eV Å^{-1}, the other (strong defects) with a pinning force F_s equal to 2 eV Å^{-1}. In this way, the effect of superposing two hardening-contributions, with different F_s/F_w ratios, from 10 to 1.33, was explored. The concentration was made to vary in two ways, i.e. in one case both defect populations had always the same concentration ($C_w/C_s = 1$); in the other, the population of strong defects was kept at a constant concentration of 10^{21} m^{-3} and only the concentration of weak defects was increased up to 10^{24} m^{-3} ($C_w/C_s = 1$–1000). For each pair of values of the ratios F_s/F_w and C_w/C_s, the simulation was repeated 50 times with different random spatial distributions of the obstacles, taking the mean maximum shear stress increase as the reference $\Delta\sigma_{tot}$. Finally, the calculated contributions of the weak and strong obstacles to the measured shear stress increase were determined by fitting S using Eq. (3).

In Fig. 1a the superposition parameter S is shown as a function of the concentration of the two defect populations (same concentration for both) and the ratio F_s/F_w. No monotonic trend with con-
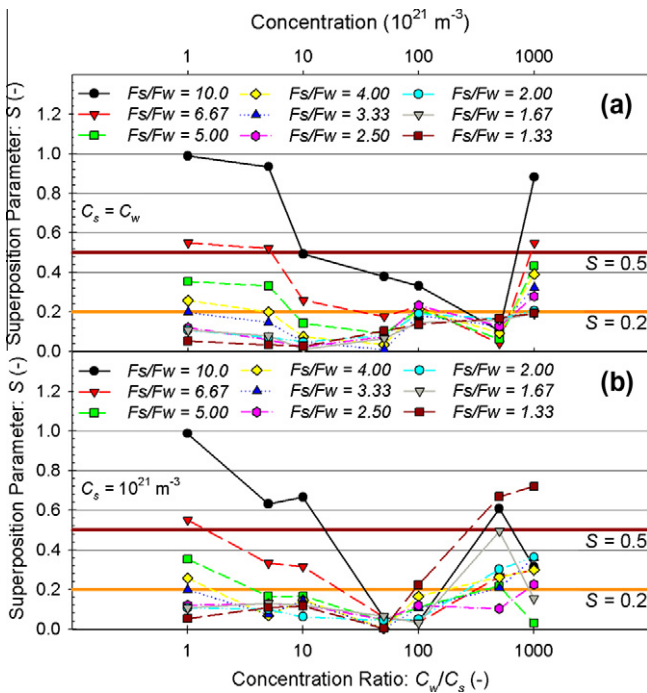

Fig. 1. (a) Superposition factor as a function of concentration and F_s/F_w ratio, for two populations of defects of equal concentration. (b) Superposition factor as a function of C_w/C_s ratio and F_s/F_w ratio, for two populations of defects.

centration is exhibited. However, it can be seen that, with the notable exception of large F_s/F_w ratios and extreme (very low or, to a lesser extent, very high) concentrations, the total shear stress increase is fairly well estimated by the quadratic summation. The superposition parameter is much more frequently closer to 0 than it is to 1. In fact, it can be said that the only case where a sensible deviation from the general trend is visible is $F_s/F_w = 10$, which corresponds indeed to a limiting case, where the effect of the weak defect population is essentially negligible and it is as if only the strong defect population was present. Very similar considerations apply to Fig. 1b, where the same quantities as in Fig. 1a are plotted in the case of a varying concentration ratio C_w/C_s.

In the following, therefore, a quadratic superposition is always assumed, except for the case where a very weak type of defects is present. In the latter case, their contribution is added linearly.

3. Evaluation of defect population strength based on the Orowan-theory and experimental results

In this part, the hardening is calculated starting from experimental results concerning the evolution of the microstructure of the alloys under irradiation. Simple calculations, using the Orowan equation are performed to provide a first notion of the strength of the different defect populations. These calculations have been performed for several model alloys.

3.1. Materials and irradiation conditions

Starting from electrolytic iron, four additional model alloys of growing chemical complexity were fabricated, i.e. Fe–0.1% Cu, Fe–0.3% Cu, Fe–Mn–Ni and Fe–Mn–Ni–Cu. They were prepared using argon-arc melting and zone refinement methods. The resulting ingots were cold worked after austenisation tempering (3 h at 1320 K), and a final heat treatment at 1075 K (during 1 h) was performed to release the stresses and to get well re-crystallized materials, followed by water quenching. Table 1 lists the chemical composition of the alloys.

Specimens of these materials, together with specimens of a 16MND5-type RPV steel, added for comparison, were irradiated in the test reactor BR2 at SCK•CEN up to a damage of about 0.1 displacements per atom (dpa) at a neutron flux of about 1.3×10^{-7} dpa s^{-1}. During irradiation the temperature and the pressure were maintained constant at respectively 573 K and 15 MPa, thereby mimicking the conditions encountered in a reactor. Here the specimens irradiated to 0.1 dpa are considered, what corresponds to the displacement dose of the planned lifetime of western NPPs.

3.2. Measurements and analysis

All measurements were performed within the European PERFECT project and are summarized in [14]. Detailed publications of these results are published elsewhere [19–22].

The tensile properties of the materials, before and after irradiation, were measured, using specimens with a gauge length of 15 mm and a diameter of 3 mm. All measurements were performed at room temperature, with a strain rate of about 2×10^{-4} s^{-1}. In Fig. 2, the data for the change in yield strength (ΔYS) as a function of the square root of the dose, expressed in *mdpa*, are plotted. With all the uncertainties and allowing for the limited statistics, one trend seems clear: in pure Fe, and Fe–Cu alloys there is a clear saturation of radiation-induced hardening visible already at very low dose. While in the case of the materials containing Ni and Mn, this dependence is rather linear. The hardening does not saturate up to the highest investigated dose, in these alloys.

Positron lifetime measurements (PAS) were performed, using the same procedure as described by Jardin et al. [23]. These measurements provide information on the size and density of small vacancy-type defects. Using the methodology proposed by Vehanen et al. [24], the size and density of the defects has been estimated [25].

Transmission electron microscope characterization (TEM) [6] was used to extract self-interstitial loop size distribution and density.

Atom-probe tomography analyzes (APT) [26] enabled the determination of the atomic-scale chemical microstructure of the material to be reconstructed in three dimensions. In fact, defect clusters of even only a few atoms can thereby be detected, but only small volumes are accessible, on the order of the tenth of thousand of nm^3. Thus, features with a number density less than 10^{22} m^{-3} cannot be detected. In addition, for the interpretation of the reconstructed volume [20], only clusters containing a minimum of five solute atoms were considered. Taking account of a detector efficiency of about 50%, this corresponds to 10 solute atoms per cluster in the real material. Thus, very small clusters, containing less than 10 solute atoms, are not considered.

And finally, small angle neutron scattering experiments (SANS) [9] provided complementary information to all the other techniques, being sensitive mainly to precipitates and voids above a certain size (∼1 nm) and requiring for the analysis a few assumptions to be made, based also on the results of the application of the other techniques.

In conclusion, it is known that each technique provides the number density and the mean size of the microstructural feature to which it is sensitive.

3.3. Results and discussions

In a first attempt, it was tried if it is possible to correlated the hardening with the results of only one technique. A scatter plot of the complete set of measured yield stress increase [19] versus square root of volume fraction deduced from SANS is shown in Fig. 3. The yield stress increase can be empirically decomposed into three components. Component (1) is due to objects not detected by SANS because of weak contrast (e.g. dislocation loops as detected by TEM) or small size (e.g. clusters of size below the detection limit of SANS as detected by APT or PAS) and not correlated with SANS.

Table 1
Chemical composition of the six different alloys in at %.

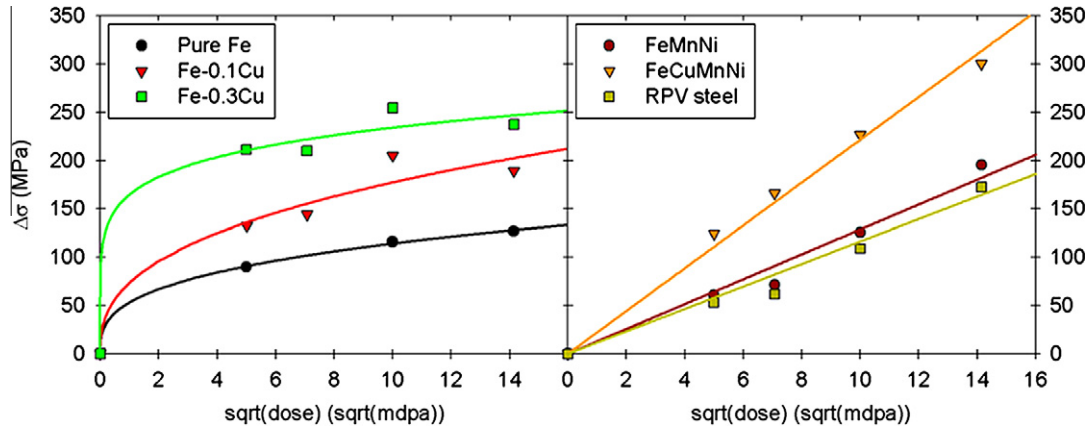| Material	Elemental concentration in at %							
	C	N	Si	P	S	Mn	Ni	Cu
Pure Fe	<0.01	<0.004	<0.01	<0.009	<0.009	0.010	<0.005	<0.005
Fe–0.1% Cu	<0.01	–	<0.01	<0.009	<0.009	0.007	<0.005	0.096
Fe–0.3% Cu	<0.01	–	0.024	<0.009	<0.009	0.010	<0.005	0.276
Fe–Mn–Ni	<0.01	<0.004	<0.01	0.009	<0.009	1.11	0.71	<0.005
Fe–Mn–Ni–Cu	<0.01	<0.004	<0.01	<0.009	<0.009	1.10	0.68	0.092
RPV steel	0.65	0.28	0.385	0.013	0.010	1.32	0.71	0.056

Fig. 2. The variation of the shift of yield stress as function of the dose square root.
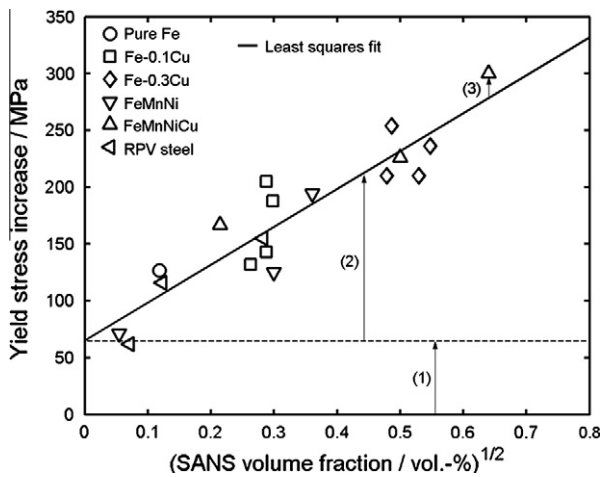

Fig. 3. Correlation between yield stress increase and volume fraction obtained by SANS assuming non-magnetic scatterers and formal decomposition into three components.

tion detected by PAS is understood to correspond to small vacancy clusters and voids, associated or not with solute atoms [19].

The objects detected by APT are, on the other hand, unambiguously known to be precipitates, whose composition is reliably provided by the technique. Nevertheless, APT cannot detect the presence of vacancies associated with the observed precipitates, if they are present. The precipitate sizes obtained from the APT are however assumed to be closer to the real ones [8].

The SANS defects appear to have a bigger mean size than it is observed by APT, while their number density is a little lower. This can be explained by the fact that very small defects, resolvable by APT, were not detected by SANS. The SANS lateral detection limit (~1 nm) is larger than the one of APT (several atoms). Nevertheless, APT and SANS results are still in good agreement, and it can therefore be assumed that they correspond mainly to the same defect populations [21].

But on the other hand, the defects visible by TEM do not correspond to any of the previous categories. These TEM defects are known to be mainly self-interstitial atom (SIA) loops, limited to those of size larger than 2 nm. Indeed, the accepted resolution limit for TEM images is about 1.5 or 2 nm. On top of this, Cu precipitates smaller than 2 nm show a bcc structure, coherent with the matrix, and therefore they will show no contrast in TEM images [6].

To illustrate the above described trends, some results from [14] are depicted in Fig. 4. It can be well seen that the defect density obtained by TEM is about two orders of magnitude lower than those obtained by the other techniques, while the size of the defects detected by PAS are much smaller compared to other sizes.

The contribution of each class of defects to the hardening can be estimated using the Orowan equation:

$$\Delta\sigma = \alpha \cdot M \cdot G \cdot b \cdot \sqrt{N \cdot d} \tag{4}$$

Here M is the Taylor factor (equal to 3.06), G is the shear modulus (71.8 GPa) and b is the module of the Burgers vector (0.249 nm). N and d are, respectively, the number density of defects and their mean size, as obtained from the experimental methods described above. The obstacle strength is given by the constant α. This value can vary between zero and one, and it is strongly dependent on the type of defect.

The hardening-contribution due to visible loops can be estimated inserting the TEM results in Eq. (4). The contribution to the hardening of the voids, on the other hand, can be obtained using the results of PAS. In pure iron, loops and nanovoids are the only two defect populations observed, and the total hardening will be given by the square root of the sum of the squares of the two contributions, as both loops and voids are assumed to be rel-
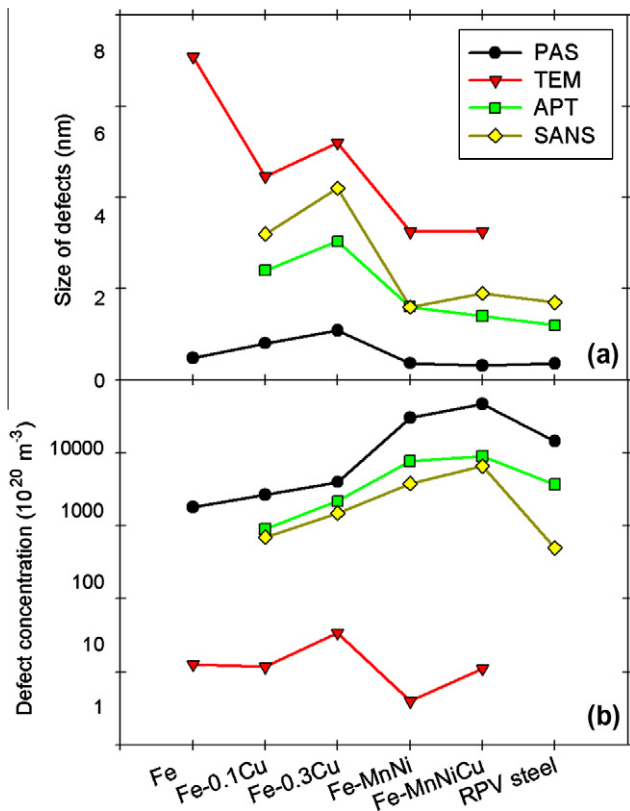
Component (2) consists of a yield stress increase directly caused by the scatterers detected by SANS and a yield stress increase caused by objects not detected by SANS but correlated with those. Component (3) may be due to measuring errors and variations of the obstacle strength of the clusters and may be associated with either component (1) or component (2).

Nevertheless, it is unlikely that component (1) will be independent of dose and material composition. Also the obstacle strength can change according to the different defect sizes. It is therefore clear that this method of defining the hardening only with one technique may give a first indication, but it will not result in a full understanding of the effect of the different classes of defects on the hardening. Therefore, in this paper, an attempt is made to add all observed defects in a correlation with the hardening results.

First, the possible defects observed by the different techniques should be listed.

It is known that some alloying elements, mainly copper, and vacancies cluster together [19,27]. Nevertheless, the size obtained from the lifetime measurement with PAS reflects the amount of vacancies only. These "mixed" clusters are therefore expected to be bigger obstacle for dislocations, than estimated from PAS results. At the same time, however, with positrons it is possible to see all kind of defects containing vacancies, even only a few vacancies close to foreign elements are detectable. These types of defects cannot be resolved by any other technique. So, the defect popula-

Fig. 4. The mean size (a) and number density (b) of the defects detected by the different experimental techniques in the different materials after irradiation to a dose of 0.1 displacements per atom.

Fig. 5. (a) The obstacle strength from Eq. (4) of the different types of defects in the investigated alloys. (b) The hardening-contribution of the different types of defects in function of the hardening measured by the tensile tests.

atively strong obstacles, of similar strength. In the Fe–Cu alloys, vacancies and copper atoms cluster together [26,28]. The size and number density of these vacancy-copper clusters the APT results are used. Also in this case, the total hardening is the square root of the sum of the squares of the two contributions (the loops and the vacancy-copper clusters).

For the alloys containing nickel and manganese some precipitates are formed, as revealed by APT, but PAS results suggest that most vacancies are not inside, but rather outside the precipitates, forming very small clusters trapped by solute elements [19]. These latter are very small defects and will thus have also a low contribution to the hardening. For the precipitates the APT results are used, while for the very small alloying-element-vacancy defects the number density is given by the difference between the PAS and the APT, and the mean size is given by PAS. In this case, there are thus three contributions, i.e. loops, precipitates and very small vacancy clusters. The first two contributions are superposed quadratically, while the contribution of the very small vacancy clusters, which are much weaker obstacles, is added linearly to the composition of the other two contributions.

The α-values from Eq. (4) for each population were fitted using the following two assumptions. First, the strength of the loops is assumed to be linearly dependent on their size. Secondly, it was assumed that the (pure) vacancy clusters containing less than 10 vacancies were negligible in strength, if any other type of defect is present as well. Therefore, the voids found in pure iron, and the small vacancy clusters observed in the alloys containing nickel and manganese were neglected in first assumption. However, it was found in [14], where the results for all four different techniques were published in more detail, that some bigger vacancy-type of defects are found in iron for other irradiation conditions. As no data were available for the irradiation dose examined in this
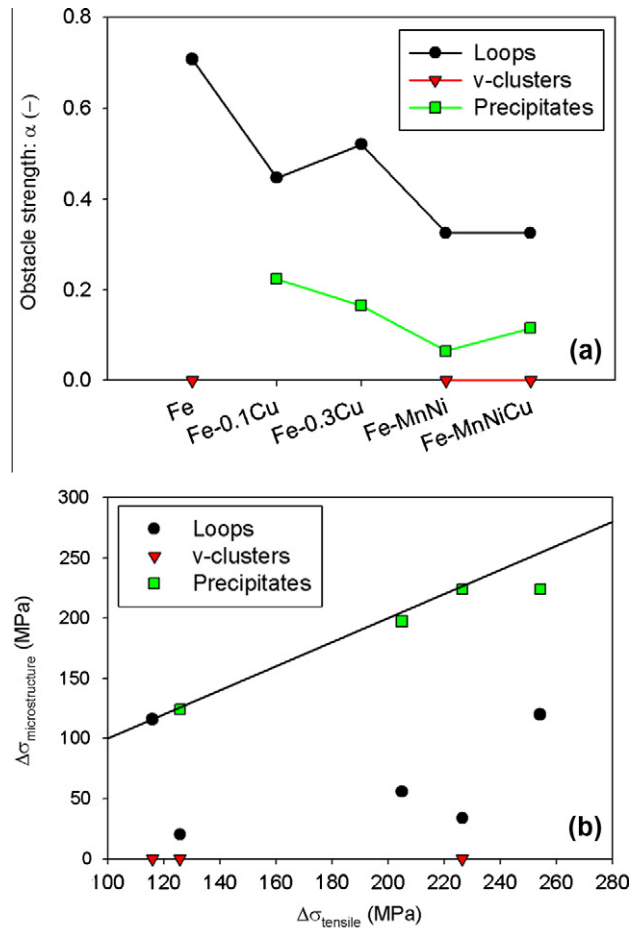
paper, they were not taken into account. Therefore, the obstacle strength attributed to the loops constitutes an upper bound.

The best fit values, using these estimations, are shown in Fig. 5a. The different hardening-contributions of the different defect populations and the total values are given in Fig. 5b. The results of the RPV steel are not given as no loops were detected by TEM. It is however expected that invisible loops are present in the steel, which have a certain contribution to the hardening.

In Fig. 5, it can be observed that the SIA loops are the strongest obstacles in the investigated alloys, but their influence on the hardening is limited due to their low density. The precipitates are found to be very small in size, what makes them behave as rather weak obstacles. However, their high density determines that they are the main hardening features. The small vacancy clusters (called v-clusters in Fig. 5) have a very low strength and a negligible contribution to the hardening, due to their small size.

4. Conclusions and outlook

A parametric study performed using a tension-line code, DU-PAIR, indicates that a quadratic superposition of the hardening of different types of defects is mostly the most appropriate one. Only when one type of defects is much softer than the other ones, the linear summation of the hardening components is better.

The combination of four experimental techniques for microstructural characterization, namely PAS, APT, SANS and TEM, leads to a good comprehension of all defect populations created by irra-

diation inside the model alloys studied in the present work. The TEM results informs about the self-interstitial loops created during irradiation. A combination of PAS and APT leads to an understanding of the irradiation-induced voids and precipitates in the alloys, while SANS is used as confirmation technique for APT and PAS findings. A sensitively assessment of the strength associated with the different defect populations, using the Orowan equation for each contribution, and their combination using the proper superposition law, provides a reasonable rationalization of the hardening results.

In the future, more precise results are expected to be obtained by using more sophisticated models, such as the suite of codes developed within the PERFECT project, i.e. RPV-2.

Acknowledgement

References

[1] G.R. Odette, G.E. Lucas, JOM 53 (7) (2001) 18–22.
[2] S.B. Fisher, J.E. Harbottle, N. Aldridge, Philos. Trans. R. Soc. Lond. A 315 (1985) 301–332.
[3] G.R. Odette, Scripta Metall. 17 (10) (1983) 1183–1188.
[4] J.T. Buswell, W.J. Phythian, R.J. McElroy, S. Dumbill, P.H.N. Ray, J. Mace, R.N. Sinclair, J. Nucl. Mater. 225 (1995) 196–214.
[5] R.G. Carter, N. Soneda, K. Dohi, J.M. Hyde, C.A. English, W.L. Server, J. Nucl. Mater. 298 (2001) 211–224.
[6] M.L. Jenkins, M.A. Kirk, Characterisation of radiation damage by transmission electron microscopy, Institute of Physics series in microscopy in materials science, 2001.
[7] M. Lambrecht, A. Almazouzi, J. Nucl. Mater. 385 (2009) 334–338.
[8] E. Meslin, PhD thesis at Université de Rouen, 2007.
[9] F. Bergner, A. Ulbricht, M. Hernandez-Mayoral, P.K. Pranzas, J. Nucl. Mater. 374 (2008) 334–337.
[10] <http://www.fp6perfect.net>.
[11] A.J.E. Foreman, M.J. Makin, Canad. J. Phys. 45 (1967) 511–517.
[12] C. Domain, L. Malerba, G. Monnet, K. Verheyen, S. Jumel, J.C. van Duysen, in: Proceedings of the 2nd Intl. Conf. on Multiscale Materials Modelling (MMM-2), N.M. Ghoniem editor, October 11–15, 2004, Los Angeles, California, USA (Mechanical & Aerospace Eng. Dept., UCLA), p. 519.
[13] S. Jumel, J.C. van Duysen, J. Ruste, C. Domain, J. Nucl. Mater. 346 (2005) 79–97.
[14] E. Meslin, M. Lambrecht, M. Hernández-Mayoral, F. Bergner, L. Malerba, P. Pareige, B. Radiguet, A. Barbu, D. Gómez-Briceño, A. Ulbricht, A. Almazouzi, J. Nucl. Mater. 406 (2010) 73–83.
[15] J.P. Hirth, J. Lothe, Theory of Dislocations, second ed., New York: Wiley, 1982.
[16] E.D. Eason, J.E. Wright, G.R. Odette, NUREG/CR-6551 (1998).;
M. Kirk, presented at EPRI MRP/NRC PTS Re-Evaluation Meeting, Rockland, Maryland, 2000.
[17] R. Chaouadi, R. Gérard, J. Nucl. Mater. 345 (2005) 65–74.
[18] G.R. Odette, G.E. Lucas, G. Tedeski, B.D. Wirth, Fusion Materials Semiannual Progress Report for Period Ending, 1998, p. 221. <http://www.ms.ornl.gov/programs/fusionmatls/pdf/dec1998/221-226.pdf>.
[19] M. Lambrecht, L. Malerba, A. Almazouzi, J. Nucl. Mater. 378 (2008) 282–290.
[20] E. Meslin, B. Radiguet, P. Pareige, A. Barbu, J. Nucl. Mater. 399 (2010) 137–145.
[21] F. Bergner, M. Lambrecht, A. Ulbricht, A. Almazouzi, J. Nucl. Mater. 399 (2010) 129–136.
[22] M. Hernández-Mayoral, D. Gómez-Briceño, J. Nucl. Mater. 399 (2010) 146–153.
[23] M. Jardin, M. Lambrecht, A.A. Rempel, Y. Nagai, E. van Walle, A. Almazouzi, Nucl. Instr. Meth. A 568–572 (2006) 716–722.
[24] A. Vehanen, P. Hautojärvi, J. Johansson, J. Yli-Kauppila, Phys. Rev. B 25 (1982) 762–780.
[25] M. Lambrecht, A. Almazouzi, J. Phys.: Conf. Ser., in press.
[26] M.K. Miller, Atom Probe Tomography, Plenum Publisher, Kluwer Academic, 2000.
[27] Y. Nagai, Z. Tang, M. Hasegawa, T. Kanai, M. Saneyasu, Phys. Rev. B 63 (2001) 134110 (1–5).
[28] K. Verheyen, M. Jardin, A. Almazouzi, J. Nucl. Mater. 351 (2006) 209–215.